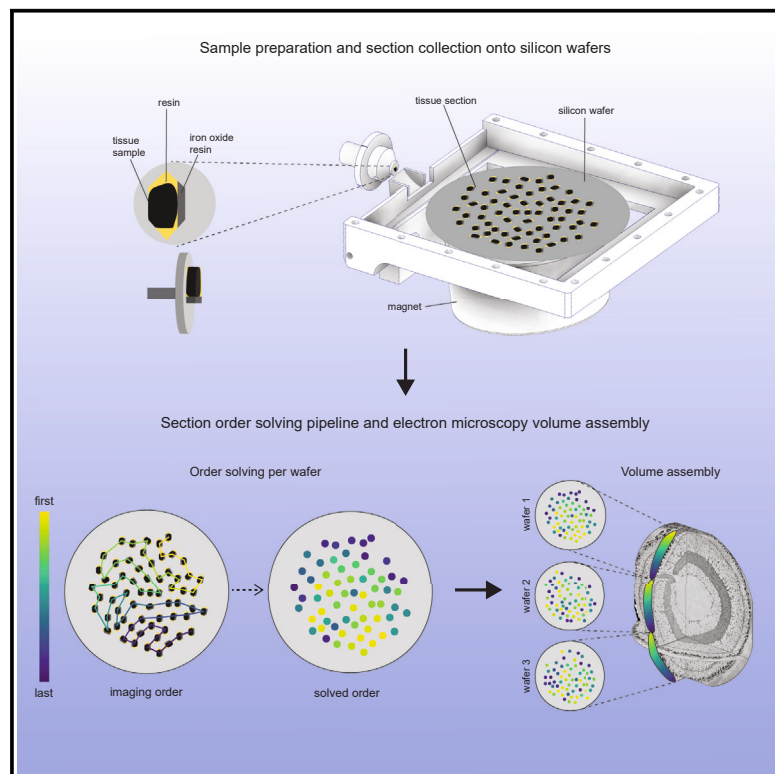


# GAUSS-EM, guided accumulation of ultrathin serial sections with a static magnetic field for volume electron microscopy

## Graphical abstract



## Authors

Kara A. Fulton, Paul V. Watkins,  
Kevin L. Briggman

## Correspondence

kevin.briggman@mpib.mpg.de

## In brief

Fulton et al. present a simple and inexpensive method to collect ultrathin tissue sections for volumetric electron microscopy. They demonstrate improved sample preparation that allows high-throughput acquisition of sections using static magnetic fields. After collection, sections are reordered and assembled into high-resolution datasets that can be used for further analysis.

## Highlights

- Improved sample preparation to embed tissues next to dense iron oxide particles
- High-throughput automated method to collect ultrathin sections using static magnetic field
- Simple and inexpensive method for acquisition of volume electron microscopy datasets



## Report

# GAUSS-EM, guided accumulation of ultrathin serial sections with a static magnetic field for volume electron microscopy

Kara A. Fulton,<sup>1,2</sup> Paul V. Watkins,<sup>1</sup> and Kevin L. Briggman<sup>1,3,\*</sup>

<sup>1</sup>Department of Computational Neuroethology, Max Planck Institute for Neurobiology of Behavior – caesar, 53175 Bonn, NRW, Germany

<sup>2</sup>Present address: Department of Neurobiology, Harvard Medical School, Boston, MA 02115, USA

<sup>3</sup>Lead contact

\*Correspondence: [kevin.briggman@mpinb.mpg.de](mailto:kevin.briggman@mpinb.mpg.de)

<https://doi.org/10.1016/j.crmeth.2024.100720>

**MOTIVATION** Volumetric electron microscopy has benefited from several forms of automation in recent years, including block-face methods such as serial block-face SEM and serial sectioning approaches such as ATUM and MagC. The ability to generate large-scale EM-based connectomic datasets is, however, still limited to a handful of labs and institutions due to the cost and complexity of implementing these methods. GAUSS-EM was developed to improve upon existing serial sectioning approaches and to expand the ability to collect large 3D anatomical volumes to a broader range of labs.

## SUMMARY

Serial sectioning electron microscopy (EM) of millimeter-scale three-dimensional (3D) anatomical volumes requires the collection of thousands of ultrathin sections. Here, we report a high-throughput automated approach, GAUSS-EM (guided accumulation of ultrathin serial sections-EM), utilizing a static magnetic field to collect and densely pack thousands of sections onto individual silicon wafers. The method is capable of sectioning hundreds of microns of tissue per day at section thicknesses down to 35 nm. Relative to other automated volume EM approaches, GAUSS-EM democratizes the ability to collect large 3D EM volumes because it is simple and inexpensive to implement. We present two exemplar EM volumes of a zebrafish eye and mouse olfactory bulb collected with the method.

## INTRODUCTION

The collection of volumetric electron microscopy (EM) data has benefited from several forms of automation.<sup>1–7</sup> These advances can be subdivided into block-face methods that serially ablate tissue within the vacuum chamber of a scanning electron microscope (SEM; serial block-face SEM [SBF-SEM], focused ion beam SEM [FIB-SEM], broad ion beam SEM [BIB-SEM])<sup>1,4,5,7,8</sup> and serial sectioning methods in which ultrathin sections are first collected and then imaged post hoc (automatic tape-collecting ultramicrotome [ATUM],<sup>3</sup> magnetic collection [MagC]<sup>6</sup>). Block-face methods can ablate tissue down to a few nanometers, allowing isotropic resolution in the lateral and axial dimensions, but destroy the sample during acquisition and require specialized microtomes<sup>1</sup> or ion beams<sup>4,5,7,8</sup> to be integrated into SEMs. Serial sectioning methods, on the other hand, are limited in minimal section thickness to approximately 30–50 nm<sup>9</sup> but benefit from a decoupling of the sectioning and imaging phases of data acquisition. That is, after sectioning, section quality can be assessed before a decision is made to proceed with imaging a specimen.

While serial sectioning has been performed by manual ultramicrotomy for decades,<sup>10,11</sup> ATUM and MagC were introduced to automate the collection of sections directly onto conducting substrates. ATUM incorporates a conveyor-belt-like pickup system to collect sections onto expensive conductive tape that is subsequently assembled on silicon wafers.<sup>3</sup> An alternative approach, MagC, mitigates the manual wafer assembly of ATUM and increases the packing density of sections on silicon wafers by utilizing a moving magnet to collect sections containing superparamagnetic nanoparticles.<sup>6</sup> However, several limitations remain with this method. Magnetic particles were mixed at a low concentration in a resin and glued onto a tissue sample block, which can, in practice, lead to a separation of the particles from the section and potential section loss. Sectioning at thicknesses down to 35 nm, a thickness typically required for accurate dense reconstruction in connectomics,<sup>12</sup> has also not been reported with MagC, nor for series of more than a few hundred sections. Finally, like ATUM, the use of motorized actuators leads to an increased complexity and cost of customizing commercial ultramicrotomes.



We sought to improve upon the MagC method to enable the collection of the thousands of 35 nm sections required to scale up to millimeter-scale anatomical volumes by optimizing sample preparation, device design, and automation. Our approach, GAUSS-EM (guided accumulation of ultrathin serial sections-EM), uses a static magnetic field to collect sections containing iron oxide nanoparticles onto silicon wafers. Like MagC, this method reduces consumable expenses compared to conductive tapes used in ATUM<sup>13</sup> and increases the packing density of sections nearly 10-fold. The major advances over MagC are an improved method for dispersing magnetic nanoparticles in resin, the use of a static magnetic field below or above a collection boat, and the demonstration of continuous serial sectioning across many thousands of sections at 35 nm. Our approach enables the collection of large volumes of ultrathin sections with minimal manual intervention at 3–4 times faster sectioning speeds than those previously reported<sup>6,14</sup> and at a substantially reduced cost.

## RESULTS

We first developed a method to disperse iron oxide particles at a high concentration in the same epoxy resin in which tissue samples were embedded to avoid an interface between two different resins as in MagC. We found that both mechanical mixing and bath sonication were insufficient to disperse the particles, but the use of a probe sonicator in which heat was dissipated during mixing was able to disperse the particles up to a concentration of 30% (w/w) in resin within 30 min (Figures 1A and S1). The iron/resin mixture was not monodisperse but contained clusters of iron oxide approximately 1 μm in diameter. The mixture was then deposited into a cavity next to a previously embedded tissue sample and polymerized (Figure 1B). The iron concentration and the cross-sectional area of iron/resin exposed when trimming the sample block face were optimized such that 35 nm sections, our target section thickness for connectomic reconstruction, were passively pulled away from the edge of the diamond knife beneath a neodymium magnet suspended above the knife boat. Importantly, we found that a 30% concentration of iron nanoparticles was necessary to enable the passive collection of sections and avoid the need for a moving magnet to collect sections, as in MagC. We typically form a hexagonal block face that includes a 250-μm-wide region of iron/resin oriented to the right of 500- to 1,000-μm-wide tissue samples, leading to an iron:tissue block-face ratio substantially below the 50:50 ratio reported for MagC<sup>6</sup> (Figure 1C).

We next explored two configurations to collect sections with a static magnetic field (see Data S1 and S2), one in which a cylindrical magnet was positioned below a custom boat (configuration 1, Figure 1D) or in which a spherical magnet was suspended above a boat (configuration 2, Figure S2A). For repeatable positioning of the magnets, we quantified the magnetic field strength distribution at the boat surfaces (Figures 1E and S2B). For both configurations, a hydrophilized silicon wafer was submerged in the water prior to sectioning on a downward slope oriented toward the front of the boat. During cutting, sections floated to the region of the highest magnetic field strength and remained

suspended in position. After cutting, water was withdrawn from the boat as sections were held in place by the magnetic field until deposition on the wafer (Figure 2A; Video S1). The magnetic field was necessary to hold the sections in place; in the absence of the field, sections dispersed when the water was withdrawn (Figure 2A). For shorter series of sections (<1,000), configuration 2 is preferred because the spherical magnet can be positioned close to the diamond knife edge, leading to a stronger pull of sections. A limitation of this configuration is that the magnet obscures the view of sections and thus a mirror is required to visualize sections from below (Figure S2A).

We prefer configuration 1 for longer series of sections (>1,000) because the use of a larger 100 mm diameter wafer allows thousands of sections to be densely packed onto a wafer and offers an unobstructed view of the sections during collection. An additional benefit of configuration 1 is that the surface of the boat is covered with a transparent sheet of plastic during sectioning to limit evaporation of water from the boat. Because the size of the magnet restricts how close it can be positioned to the knife edge, we added a glass capillary that delivers a puff of air near the knife edge following each cut (see STAR Methods). The number of sections that can fit onto a 100 mm wafer depends on the section size, but in practice, we typically collect 2,000–3,000 sections on each wafer (Figures 1F and 1G). We routinely section at 0.8–1.2 mm/s, yielding a net collection rate of >1,000 sections per hour for block faces of ~1.5 mm in length.

The sequence in which sections were cut is not preserved once they float onto the water surface; therefore, the correct ordering must be determined to assemble a three-dimensional (3D) volume. Sections could, in principle, be tracked by video recording during collection, but we opted for an algorithmic method to solve for the correct ordering of sections following SEM imaging. A scale-invariant feature transform (SIFT)-based feature<sup>15,16</sup> matching algorithm was applied to regions containing tissue for every pairwise combination of 2D-stitched SEM micrographs to assemble a distance matrix among all sections on an individual wafer (Figure S3A). We then found the shortest path through this matrix using a traveling salesman problem (TSP) solver (Figure S3B; see [data and code availability](#)), equivalent to the inlier ratio method described previously.<sup>17</sup> Sections that do not contain a sufficient number of matching features for the TSP solving step can be semi-automatically placed in the correct sequence (Figure S3C). This is typically only required if the imaging contrast is significantly different from most other sections or if a section was damaged during cutting.

To assess the robustness of the algorithm, we randomly removed either 50% or 90% of sections from a sequence and re-solved the orderings (Figure S4A). In both cases, the correct ground-truth ordering was still recovered, except for two swapped sections that needed to be manually corrected when 50% of all sections were randomly removed. Given that missing such a high fraction of sections would be unlikely to yield a useful 3D EM volume anyway, we consider the order solving to be robust to missing sections. There is a dependency on the imaged field of view required to detect and match a sufficient number of SIFT features (Figure S4B). To explore this, we performed an analysis to artificially reduce the number of SIFT features in

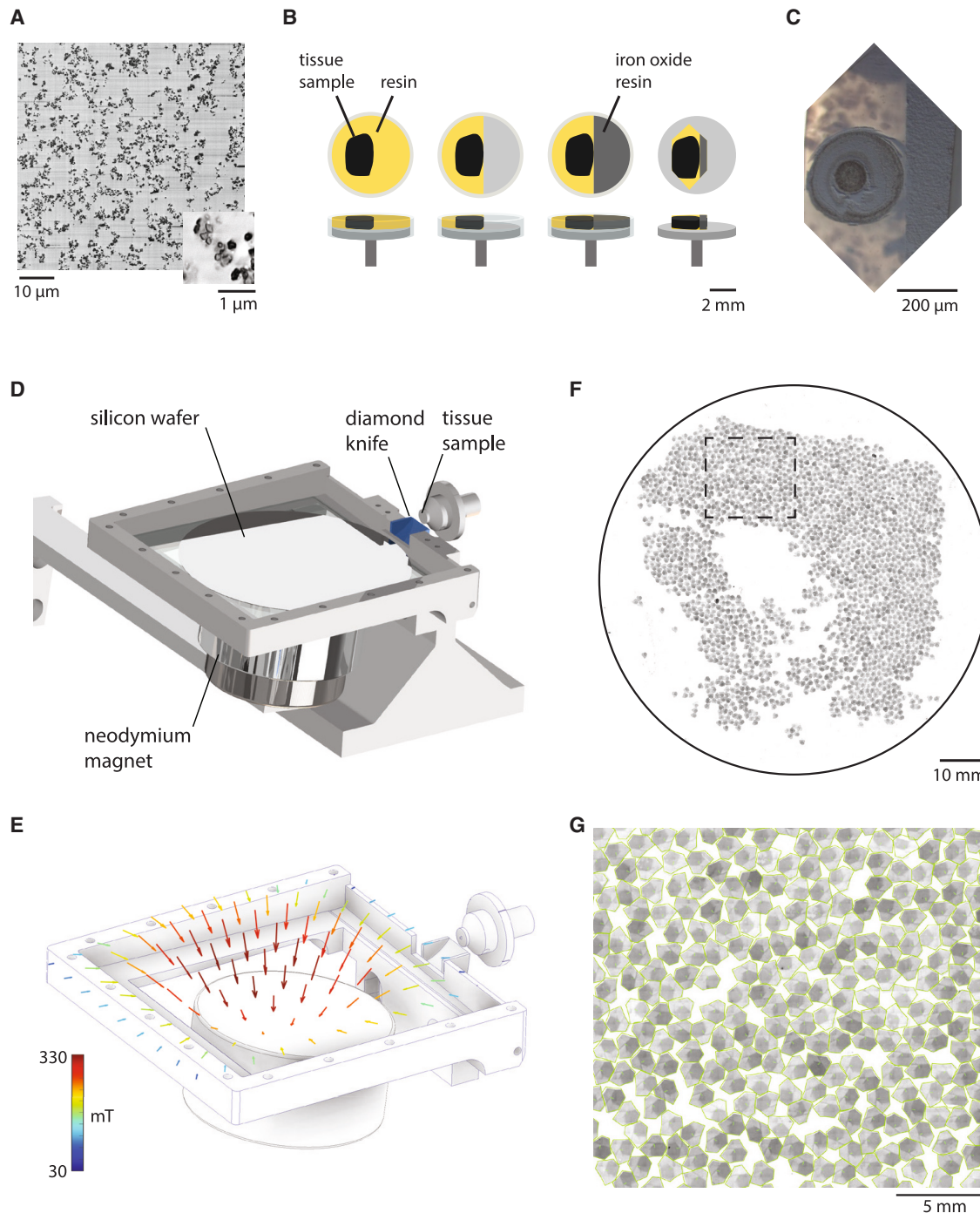


**Figure 1. Guided accumulation of ultrathin serial sections with a static magnetic field**

- (A) Electron micrograph of 30% iron oxide dispersed within resin. Inset illustrates iron nanoparticle clusters.
  - (B) Sequence of steps to adhere iron/resin mixture to tissue samples.
  - (C) Trimmed block face containing a tissue sample and iron/resin mixture.
  - (D) Configuration 1 with a custom collection boat for 100 mm silicon wafers and a cylindrical neodymium magnet.
  - (E) Magnetic field strengths at the surface of the boat.
  - (F and G) Representative image of 35 nm serial sections collected on a silicon wafer (F) and a magnified view (G).
- See also [Figures S1, S2, and S5](#) and [Data S1](#).

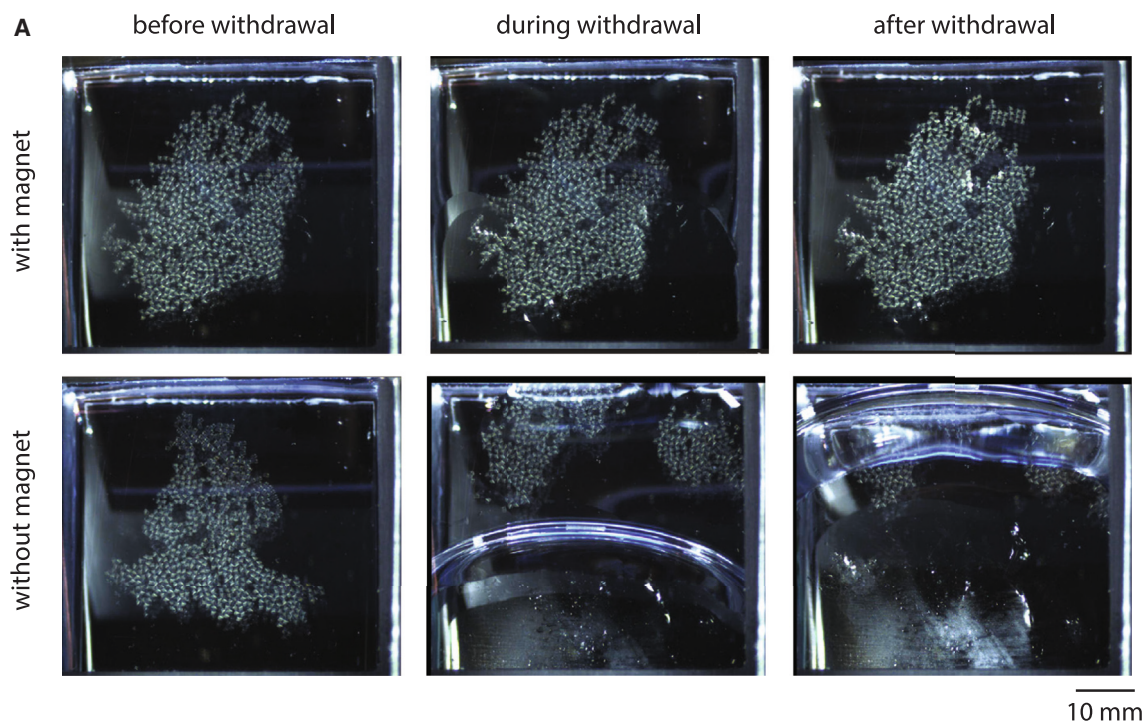


**Figure 2. Collection of sections onto silicon wafers**

(A) Illustration of the location of sections before, during, and after the withdrawal of water from the boat both in the presence of the magnet above the boat (top) and absence of the magnet (bottom). For this example, sections were collected on an ITO-coated glass wafer instead of a silicon wafer to visualize the effect of the magnetic field during water withdrawal with a camera from below.

See also [Video S1](#).

each section ([Figure S4C](#)). We found that the fraction of bad matches (i.e., sections that did not fit to an affine transformation with their neighbors) approached 100% when just 10% of detected SIFT features are randomly sampled. Importantly, there is a strong correlation between the field of view (tissue area) and the number of detected SIFT features. For the wafer with the smallest tissue area (wafer 1), the order-solving algorithm began to breakdown below 20% of randomly sampled SIFT features. The mean area for wafer 1 was approximately  $29,200 \mu\text{m}^2$ ; therefore, for this particular tissue type, sections containing less than  $5,840 \mu\text{m}^2$  of tissue area (e.g., a  $76 \times 76 \mu\text{m}$  square bounding area) would not be correctly sorted. The matching SIFT features tended to be located in areas containing large objects such as somata and blood vessels compared to neuropil regions ([Figure S4D](#)).

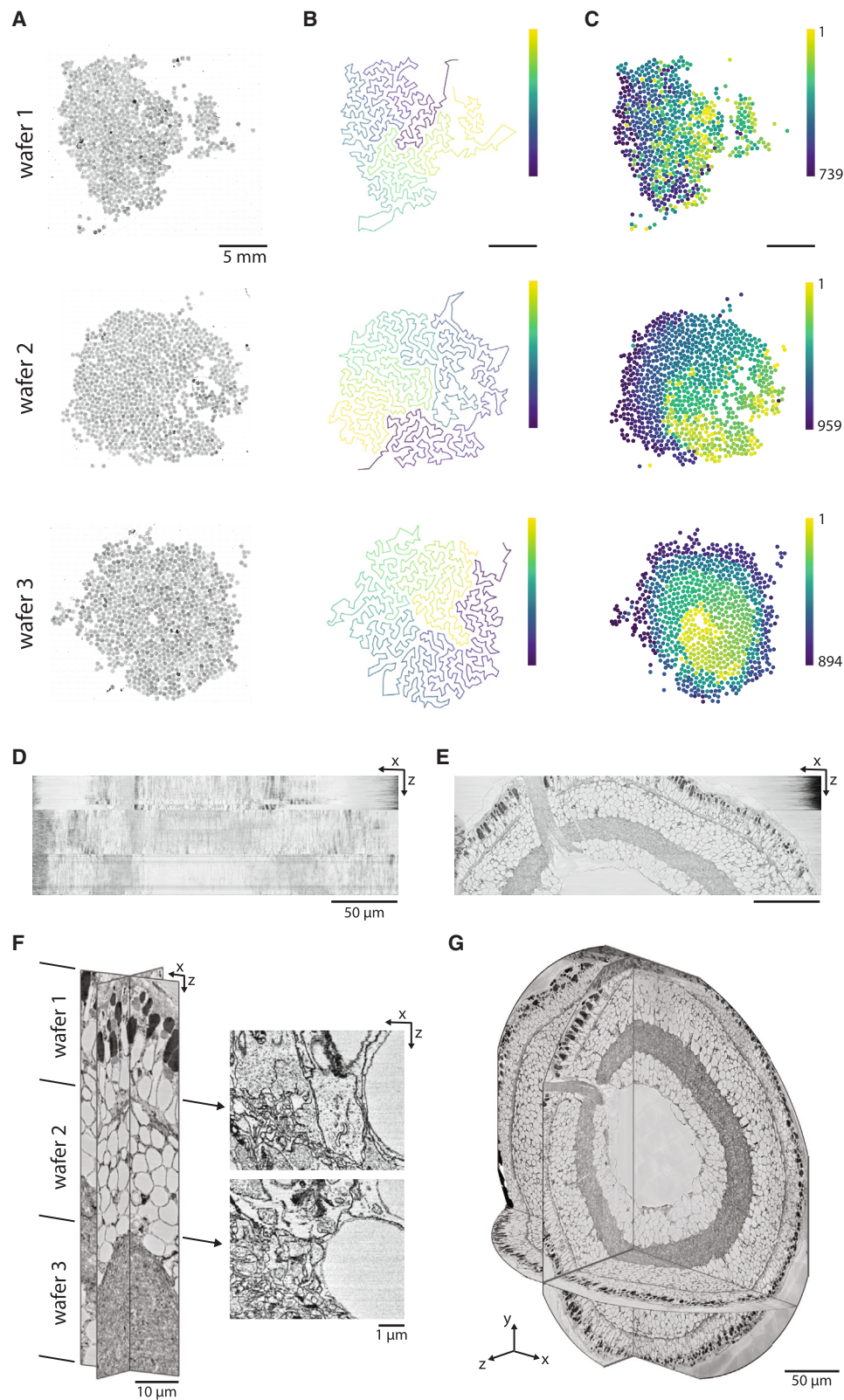
As proof of principle, we collected 3D volumes of a larval zebrafish retina (collected using configuration 2, [Figure 3](#)) and from a mouse olfactory bulb (collected with configuration 1, [Figure 4](#)). The zebrafish retina (2,592 sections) was collected on three wafer pieces ([Figure 3A](#)) and imaged in an order to minimize SEM stage movements ([Figure 3B](#)), and then the section sequence was solved ([Figure 3C](#)). An XZ virtual slice through the assembled image stack illustrates the imaging order compared to the solved order ([Figures 3D and 3E; Video S2](#)). The olfactory bulb volume (7,495 sections) was collected on four silicon wafers ([Figures 4A and 4B](#)). To assess the quality

of the volumes, we focused on the transitions between wafers and did not observe any gap in the continuity of neurites ([Figures 3F and 4C](#)).

The final aligned volumes ([Figures 3G and 4B](#)) are publicly accessible (see [data and code availability](#)).

## DISCUSSION

Overall, GAUSS-EM is the first ultramicrotomy method that automates the collection of thousands of serial sections by a passive mechanism—a static magnetic field. We routinely cut 35 nm sections at speeds that yield hundreds of microns of tissue cut within a single day. In terms of the sample yield, while we routinely prepare backup samples as a precaution, we have generally had success with the first sample and have not needed to resort to using backups. Once a sample is observed to section well (e.g., if it is uniformly well embedded in resin), we have not observed a degradation in the collection success over many thousands of sections. Ultimately, the diamond knife will become the limiting factor and, as with all sectioning approaches, will eventually need to be resharpened. We have not designed the custom boats to allow easy knife changes in the middle of an experiment; rather, we prefer to simply manufacture several boats that can be swapped out if needed during a long sectioning experiment. We estimate a minimum of 30,000 sections, conservatively, could be cut



(legend on next page)

from a ~1-mm-wide block face with a single 4-mm-wide diamond knife. For example, if a knife were moved laterally to a fresh cutting edge in 200  $\mu\text{m}$  steps every 2,000 sections, then a total movement of 3 mm (to reach the other end of a 4 mm knife) would yield 30,000 sections (equivalent to ~1 mm depth with 35 nm sections).

For the 2 datasets presented here, we had to exclude 2, 4, and 13 sections (per wafer for the zebrafish retina sample) and 2, 0, 6, and 6 sections (per wafer for the mouse olfactory bulb sample) during the order-solving pipeline. The reasons for exclusions were most commonly thin (<35 nm) sections with insufficient contrast and, more rarely, section folds. This leads to a rejected section rates of 0.73% and 0.186% for the zebrafish and olfactory bulb volumes, respectively. We think this is not a limitation of GAUSS-EM specifically but is related to the variability in sectioning that other diamond knife sectioning methods also experience. Our error rates are comparable to, or less than, those previously reported for ATUM.<sup>18</sup>

The order-solving algorithm requires the creation of an all-to-all section dissimilarity distance matrix that can be computationally demanding. In the case where access to a high-performance computing cluster containing hundreds of GPUs is not possible, we suggest reducing the computational time by (1) limiting the number of detected SIFT features (see Figure S4C) and (2) utilizing approximate k-nearest-neighbor libraries that trade off accuracy for runtime. We note that the order solving may potentially become intractable with 10,000 or more sections on a single wafer. While we have not yet found the limit, computation of the dissimilarity matrix is currently tractable with several thousand sections per wafer. The matching SIFT features were detected in images downsampled to 128 or 256 nm and tended to be located in areas containing somata and blood vessels. This is due to the SIFT-matching algorithm requiring sufficient similarity, which is provided by larger structures that do not change too much between sections. If the high-resolution target imaging region for a sample consists only of fine neuropil, we suggest imaging lower-magnification overviews (e.g., at 256 nm pixel size) that contain such larger structures.

Because the sectioning and imaging steps are decoupled, this method allows one to potentially collect sections at one institution and then image wafers at EM facilities at which high-speed SEMs<sup>19</sup> are available. The simplicity of GAUSS-EM should allow any laboratory with access to an ultramicrotome to inexpensively implement the method. In addition to the high-throughput sectioning afforded by GAUSS-EM, the deposition of sections directly onto flat silicon wafers,

compared to plastic tapes as in ATUM, allows for a reduction in the imaging overhead caused by autofocusing and autostigmation during SEM acquisition. We typically perform just one round of autofocusing and autostigmation per section, instead of the multiple rounds needed for sections mounted on tapes. To add additional information to EM volumes, GAUSS-EM can be readily combined with correlative light microscopy techniques such as pre- and post-embedding immunohistochemistry.<sup>20,21</sup> Finally, we note that GAUSS-EM is also compatible with hybrid imaging methods in which thicker (>100 nm) sections are collected onto wafers and subsequently milled with an ion beam.<sup>4,7</sup>

### Limitations of study

In addition to some of the considerations described above, GAUSS-EM shares the same limitations as other serial sectioning techniques—limited achievable minimum section thicknesses and the need to clean/resharpen the diamond knife over time. In serial sectioning approaches, the section thickness typically limits the axial resolution of the dataset and is thicker than block-face approaches. While it may be possible to collect thinner (<35 nm) sections with GAUSS-EM, we have not investigated the yield with thinner sections for large volumes.

### STAR★METHODS

Detailed methods are provided in the online version of this paper and include the following:

- KEY RESOURCES TABLE
- RESOURCE AVAILABILITY
  - Lead contact
  - Materials availability
  - Data and code availability
- EXPERIMENTAL MODEL AND STUDY PARTICIPANT DETAILS
- METHOD DETAILS
  - EM staining and resin embedding
  - Iron/resin preparation
  - Sample block preparation
  - Assembly of collection boats and sectioning procedure
  - Configuration one
  - Configuration two
  - Serial sectioning
  - SEM imaging
  - Alignment and assembly of 3D EM volumes
- QUANTIFICATION AND STATISTICAL ANALYSIS

### Figure 3. Assembly of sections into 3D volumes

- (A) Three wafers containing 35 nm sections from a larval zebrafish retina collected with configuration 2.  
(B) Sequence in which sections were imaged.  
(C) Color-coded order of the solved sequence of sections.  
(D) XZ reslice of sections in the imaging order of (B).  
(E) XZ reslice of sections in the solved order of (C).  
(F) Magnified XZ reslices, illustrating the transition between wafers 1 and 2 and wafers 2 and 3.  
(G) 3D view of the assembled larval zebrafish retina.  
See also Figures S3 and S4 and Video S2.

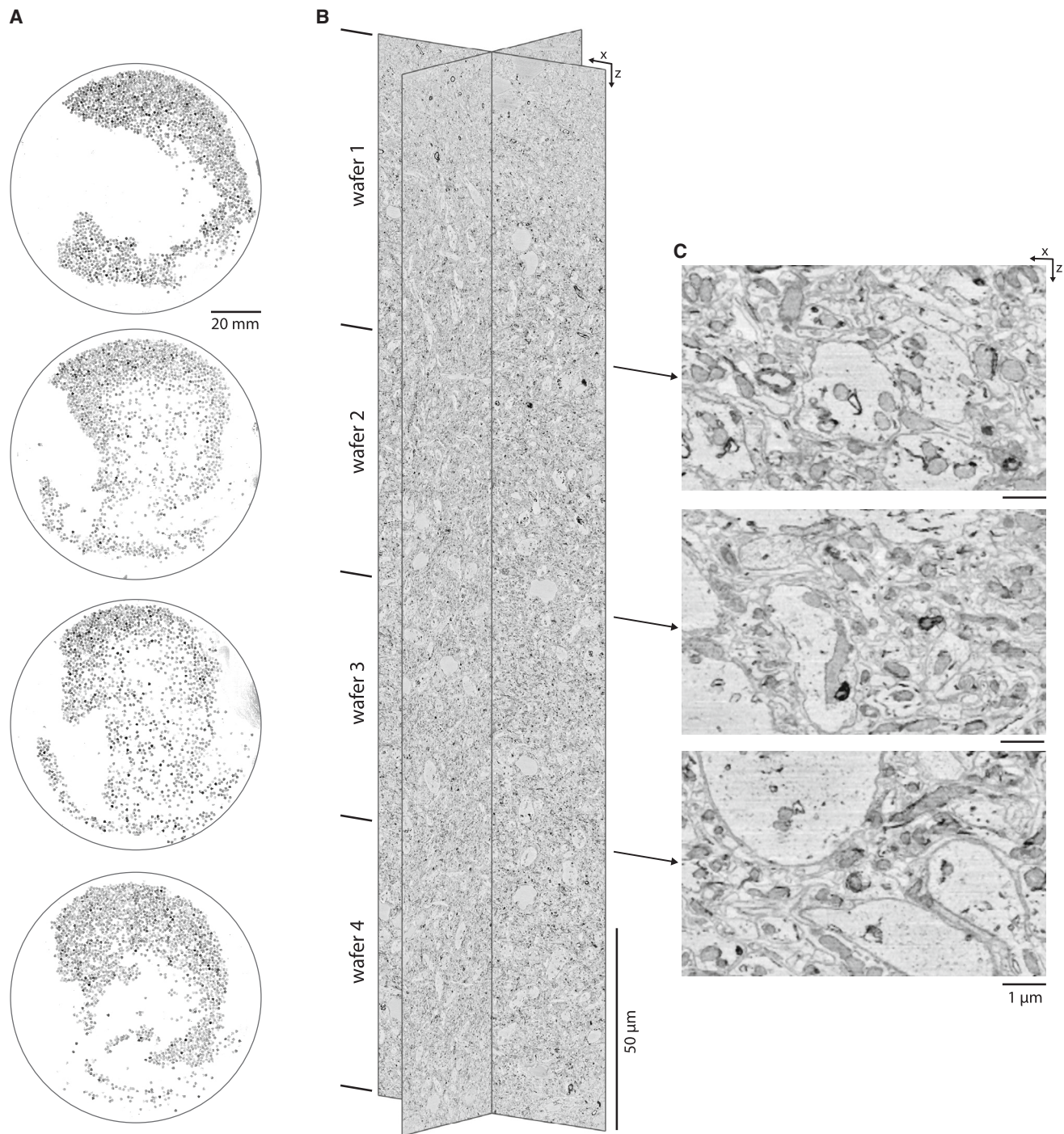


**Figure 4. An example volume from the mouse olfactory bulb**

(A) Light microscope images of sections collected on four 100 mm silicon wafers.

(B) XZ and YZ reslices through the aligned volume with the boundaries between wafers indicated.

(C) Higher-magnification XZ reslices highlighting the transition between the four wafers in the aligned volume.

#### SUPPLEMENTAL INFORMATION

Supplemental information can be found online at <https://doi.org/10.1016/j.crmeth.2024.100720>.

#### ACKNOWLEDGMENTS

We would like to thank Irene Gügel, Silke Haverkamp, Marta Pallotto, Lennart Tegethoff, and Takeshi Yoshimatsu for assistance with sample preparation.

We also thank Stephan Irzen for assistance with multibeam SEM imaging and the MPINB mechanical workshop for machining of components. Funding was provided by the Max Planck Society.

#### AUTHOR CONTRIBUTIONS

K.A.F. and K.L.B. developed the method and collected the EM datasets, and P.V.W. developed the order-solving pipeline. All authors contributed to the writing of the manuscript.

#### DECLARATION OF INTERESTS

The authors declare no competing interests.

Received: September 19, 2023

Revised: December 30, 2023

Accepted: February 9, 2024

Published: March 6, 2024

#### REFERENCES

1. Denk, W., and Horstmann, H. (2004). Serial block-face scanning electron microscopy to reconstruct three-dimensional tissue nanostructure. *PLoS Biol.* 2, e329. <https://doi.org/10.1371/journal.pbio.0020329>.
2. Briggman, K.L., and Bock, D.D. (2012). Volume electron microscopy for neuronal circuit reconstruction. *Curr. Opin. Neurobiol.* 22, 154–161. <https://doi.org/10.1016/j.conb.2011.10.022>.
3. Hayworth, K., Kasthuri, N., Schalek, R., and Lichtman, J. (2006). Automating the collection of ultrathin serial sections for large volume TEM reconstructions. *Microsc. Microanal.* 12, 86–87.
4. Hayworth, K.J., Peale, D., Januszewski, M., Knott, G.W., Lu, Z., Xu, C.S., and Hess, H.F. (2020). Gas cluster ion beam SEM for imaging of large tissue samples with 10 nm isotropic resolution. *Nat. Methods* 17, 68–71. <https://doi.org/10.1038/s41592-019-0641-2>.
5. Heymann, J.A.W., Hayles, M., Gestmann, I., Giannuzzi, L.A., Lich, B., and Subramaniam, S. (2006). Site-specific 3D imaging of cells and tissues with a dual beam microscope. *J. Struct. Biol.* 155, 63–73. <https://doi.org/10.1016/j.jsb.2006.03.006>.
6. Templer, T. (2019). MagC, magnetic collection of ultrathin sections for volumetric correlative light and electron microscopy. *eLife* 8, e45696. <https://doi.org/10.7554/eLife.45696>.
7. Gholinia, A., Curd, M.E., Bousser, E., Taylor, K., Hosman, T., Coyle, S., Shearer, M.H., Hunt, J., and Withers, P.J. (2020). Coupled Broad Ion Beam-Scanning Electron Microscopy (BIB-SEM) for polishing and three dimensional (3D) serial section tomography (SST). *Ultramicroscopy* 214, 112989. <https://doi.org/10.1016/j.ultramic.2020.112989>.
8. Knott, G., Marchman, H., Wall, D., and Lich, B. (2008). Serial section scanning electron microscopy of adult brain tissue using focused ion beam milling. *J. Neurosci.* 28, 2959–2964. <https://doi.org/10.1523/jneurosci.3189-07.2008>.
9. Schalek, R., Wilson, A., Lichtman, J., Josh, M., Kasthuri, N., Berger, D., Seung, S., Anger, P., Hayworth, K., and Aderhold, D. (2012). ATUM-based SEM for High-Speed Large-Volume Biological Reconstructions. *Microsc. Microanal.* 18, 572–573. <https://doi.org/10.1017/s1431927612004710>.
10. Bock, D.D., Lee, W.C.A., Kerlin, A.M., Andermann, M.L., Hood, G., Wetzel, A.W., Yurgenson, S., Soucy, E.R., Kim, H.S., and Reid, R.C. (2011). Network anatomy and in vivo physiology of visual cortical neurons. *Nature* 471, 177–182. <https://doi.org/10.1038/nature09802>.
11. White, J.G., Southgate, E., Thomson, J.N., and Brenner, S. (1986). The structure of the nervous system of the nematode *Caenorhabditis elegans*. *Philos. Trans. R. Soc. Lond. B Biol. Sci.* 314, 1–340.
12. Helmstaedter, M. (2013). Cellular-resolution connectomics: challenges of dense neural circuit reconstruction. *Nat. Methods* 10, 501–507. <https://doi.org/10.1038/nmeth.2476>.
13. Kubota, Y., Sohn, J., Hatada, S., Schurr, M., Straehle, J., Gour, A., Neu-jahr, R., Miki, T., Mikula, S., and Kawaguchi, Y. (2018). A carbon nanotube tape for serial-section electron microscopy of brain ultrastructure. *Nat. Commun.* 9, 437. <https://doi.org/10.1038/s41467-017-02768-7>.
14. Kasthuri, N., Hayworth, K.J., Berger, D.R., Schalek, R.L., Conchello, J.A., Knowles-Barley, S., Lee, D., Vázquez-Reina, A., Kaynig, V., Jones, T.R., et al. (2015). Saturated Reconstruction of a Volume of Neocortex. *Cell* 162, 648–661. <https://doi.org/10.1016/j.cell.2015.06.054>.
15. Lowe, D.G. (1999). Object Recognition from Local Scale-Invariant Features. *1152*, pp. 1150–1157.
16. Bradski, G. (2000). The OpenCV Library. *Dr. Dobb's Journal* 25, 120–125.
17. Hanslovsky, P., Bogovic, J.A., and Saalfeld, S. (2017). Image-based correction of continuous and discontinuous non-planar axial distortion in serial section microscopy. *Bioinformatics* 33, 1379–1386. <https://doi.org/10.1093/bioinformatics/btw794>.
18. Hildebrand, D.G.C., Cicconi, M., Torres, R.M., Choi, W., Quan, T.M., Moon, J., Wetzel, A.W., Scott Champion, A., Graham, B.J., Randlett, O., et al. (2017). Whole-brain serial-section electron microscopy in larval zebrafish. *Nature* 545, 345–349. <https://doi.org/10.1038/nature22356>.
19. Eberle, A.L., Mikula, S., Schalek, R., Lichtman, J., Tate, M.L.K., and Zeidler, D. (2015). High-resolution, high-throughput imaging with a multibeam scanning electron microscope. *J. Microsc.* 259, 114–120. <https://doi.org/10.1111/jmi.12224>.
20. Fulton, K.A., and Briggman, K.L. (2021). Permeabilization-free en bloc immunohistochemistry for correlative microscopy. *Elife* 10, e63392. <https://doi.org/10.7554/elife.63392>.
21. Micheva, K.D., and Smith, S.J. (2007). Array tomography: a new tool for imaging the molecular architecture and ultrastructure of neural circuits. *Neuron* 55, 25–36. <https://doi.org/10.1016/j.neuron.2007.06.014>.
22. Watkins, P.V., Jelli, E., and Briggman, K.L. (2023). msemalign: a pipeline for serial section multibeam scanning electron microscopy volume alignment. *Front. Neurosci.* 17, 1281098. <https://doi.org/10.3389/fnins.2023.1281098>.
23. Johnson, J., Douze, M., and Jégou, H. (2021). Billion-Scale Similarity Search with GPUs. *IEEE Trans. Big Data* 7, 535–547.
24. Pallotto, M., Watkins, P.V., Fubara, B., Singer, J.H., and Briggman, K.L. (2015). Extracellular space preservation aids the connectomic analysis of neural circuits. *Elife* 4, e08206. <https://doi.org/10.7554/elife.08206>.
25. Briggman, K.L., Helmstaedter, M., and Denk, W. (2011). Wiring specificity in the direction-selectivity circuit of the retina. *Nature* 471, 183–188. <https://doi.org/10.1038/nature09818>.
26. Glauert, A.M., and Lewis, P.R. (1998). *Biological Specimen Preparation for Transmission Electron Microscopy* (Princeton University Press).
27. Hayworth, K.J., Morgan, J.L., Schalek, R., Berger, D.R., Hildebrand, D.G.C., and Lichtman, J.W. (2014). Imaging ATUM ultrathin section libraries with WaferMapper: a multi-scale approach to EM reconstruction of neural circuits. *Front. Neural Circuits* 8, 68. <https://doi.org/10.3389/fncir.2014.00068>.
28. Applegate, D.L., Bixby, R.E., Chvatal, V., and Cook, W.J. (2003). Concorde-03.12.19. <https://www.math.uwaterloo.ca/tsp/index.html>.

## STAR★METHODS

### KEY RESOURCES TABLE

REAGENT or RESOURCE	SOURCE	IDENTIFIER
<b>Chemicals, peptides, and recombinant proteins</b>		
EMbed 812 resin	Electron Microscopy Sciences	Cat#14901
BDMA	Electron Microscopy Sciences	Cat#11400
NMA	Electron Microscopy Sciences	Cat#19001
DDSA	Electron Microscopy Sciences	Cat#13711
Iron oxide II,III nanopowder	Sigma Aldrich	Cat#637106
Osmium tetroxide (4%)	Electron Microscopy Sciences	Cat#19190
Potassium ferrocyanide	Sigma Aldrich	Cat#60279
Thiocarbohydrazide	Electron Microscopy Sciences	Cat#21900
CaCl <sub>2</sub> .2H <sub>2</sub> O	Sigma Aldrich	Cat#C7902
Sodium cacodylate trihydrate	Sigma Aldrich	Cat#20840
Uranyl acetate	Electron Microscopy Sciences	Cat#22400
Lead nitrate	Sigma Aldrich	Cat#203580
L-aspartic acid	Sigma Aldrich	Cat#A7219
Ethyl alcohol (200 proof)	Electron Microscopy Sciences	Cat#15056
Propylene oxide, EM grade	Sigma Aldrich	Cat#82320
Sodium chloride	Sigma Aldrich	Cat#S7653
KCl	Sigma Aldrich	Cat#P3911
Magnesium sulfate heptahydrate	Sigma Aldrich	Cat#230391
Sodium bicarbonate	Sigma Aldrich	Cat#S4019
Sodium phosphate, monobasic monohydrate	Sigma Aldrich	Cat#71504
Glucose	Sigma Aldrich	Cat#G7528
50% Glutaraldehyde	Electron Microscopy Sciences	Cat#16316
32% Paraformaldehyde	Electron Microscopy Sciences	Cat#15714
<b>Deposited data</b>		
Mouse olfactory bulb	This paper	<a href="https://webknossos.mpibn.mpg.de/links/2vJYQ1O3vKUhRZld">https://webknossos.mpibn.mpg.de/links/2vJYQ1O3vKUhRZld</a>
Zebrafish retina	This paper	<a href="https://webknossos.mpibn.mpg.de/links/4ig-0q1evJ649zfo">https://webknossos.mpibn.mpg.de/links/4ig-0q1evJ649zfo</a>
<b>Experimental models: Organisms/strains</b>		
Mouse: C57BL/6, male	Charles River	Strain#027
Danio rerio (zebrafish)	Takeshi Yoshimatsu	N/A
<b>Software and algorithms</b>		
Order solving algorithm	This paper	<a href="https://zenodo.org/doi/10.5281/zenodo.10533853">https://zenodo.org/doi/10.5281/zenodo.10533853</a> <a href="https://github.com/mpibn/gauss-em">https://github.com/mpibn/gauss-em</a>
msemalign	Watkins et al. <sup>22</sup>	<a href="https://github.com/mpibn/msemalign">https://github.com/mpibn/msemalign</a>
FAISS	Johnson et al. <sup>23</sup>	<a href="https://github.com/facebookresearch/faiss">https://github.com/facebookresearch/faiss</a>
opencv	Bradski <sup>16</sup>	<a href="https://opencv.org/">https://opencv.org/</a>
<b>Other</b>		
Silicon wafers	KristallTechnologies	Cat#S4974
Silicon wafers	Siegert Wafer	Cat#BO14072
Teslameter magnetometer	Projekt Elektronik Teslameter	Cat#FM3-02
Neodymium Magnet	Supermagnete	Cat#S-70-35-N
Neodymium Magnet	Supermagnete	Cat#K-40-C
Neodymium pot magnet	Supermagnete	Cat#ZTN-32
Diamond knives	Diatome	35° or 45° Ultra or Ultra Jumbo
Solenoid pinch valve	Takasago Fluidic Systems	Cat#PM-0815W

## RESOURCE AVAILABILITY

### Lead contact

Further information and requests for resources and reagents should be directed to and will be fulfilled by the lead contact, Kevin L. Briggman ([kevin.briggman@mpinb.mpg.de](mailto:kevin.briggman@mpinb.mpg.de)).

### Materials availability

This study did not generate any new unique reagents.

### Data and code availability

- This paper reports two electron microscopy volumes, which are publicly available and listed in the [key resources table](#). The zebrafish retina dataset is viewable at <https://webknossos.mpinb.mpg.de/links/4ig-0q1evJ649zfo>. The mouse olfactory bulb dataset is viewable at <https://webknossos.mpinb.mpg.de/links/2VjYQ1O3vKUhRZId>. An example for the section order solving procedure and source code is available at <https://github.com/mpinb/gauss-em>.
- The code has been deposited at Zenodo and the DOI to access this code can be found in the [key resources table](#).
- Any additional information required to reanalyze the data reported in this paper is available from the [lead contact](#) ([kevin.briggman@mpinb.mpg.de](mailto:kevin.briggman@mpinb.mpg.de)) upon request.

## EXPERIMENTAL MODEL AND STUDY PARTICIPANT DETAILS

All animal experiments were conducted in accordance with the animal welfare guidelines of the Max Planck Society and with animal experimentation approval granted by the Landesamt für Natur, Umwelt und Verbraucherschutz Nordrhein-Westfalen, Germany.

An adult (C57BL/6, strain#027) male mouse was first anesthetized with isofluorane before swift decapitation. The brain was carefully removed from the skull, and 300  $\mu$ m horizontal sections from the olfactory bulb were cut on a vibratome (Leica) and briefly stored in a cold carboxygenated (95% O<sub>2</sub>/5% CO<sub>2</sub>) ACSF solution (300–320 mOsm) containing (in mM): 124 NaCl, 3 KCl, 1.3 MgSO<sub>4</sub>·7H<sub>2</sub>O, 26 NaHCO<sub>3</sub>, 1.25 NaH<sub>2</sub>PO<sub>4</sub>·H<sub>2</sub>O, 20 glucose, 2 CaCl<sub>2</sub>·2H<sub>2</sub>O. Sections were then immersion-fixed in 4% paraformaldehyde (Electron Microscopy Sciences) and 2% glutaraldehyde (Electron Microscopy Sciences) using a protocol to preserve extracellular space.<sup>24</sup>

A 6 dpf larval zebrafish was anesthetized in 0.01% tricaine, the eyes enucleated, and immersion fixed in 2% glutaraldehyde in 150 mM cacodylate buffer overnight.

## METHOD DETAILS

### EM staining and resin embedding

The samples were stained as previously described.<sup>25</sup> Briefly, the samples were stained in a solution containing 2% osmium tetroxide, 3% potassium ferrocyanide, and 2 mM CaCl<sub>2</sub> in 150 mM CB for 2 h at 4°C, followed by 1% thiocarbohydrazide (1 h at 50°C), and 2% osmium tetroxide (1 h at room temperature). The samples were then stained with 1% aqueous uranyl acetate for 6 h at 45°C and lead aspartate for 6 h at 45°C. The tissue was dehydrated at 4°C through an ethanol series (70%, 90%, 100%), transferred to propylene oxide, infiltrated at room temperature with 50%/50% propylene oxide/Epon, and then 100% Epon. Both samples were embedded in medium hard Epon<sup>26</sup> (14120; Electron Microscopy Sciences) and cured on aluminum stubs (75638-10; Electron Microscopy Sciences) at 60°C for 24 h.

### Iron/resin preparation

We tested several iron oxide nanoparticles for their ability to disperse in epoxy resin and the strength of the magnetic pull when sectioned at 35 nm. The optimal formulation was iron oxide II,III nanopowder (50–100 nm size particles; #637106; Sigma-Aldrich). 10 mL of medium hard Epon was prepared in a 20 mL glass scintillation vial by weight but without the addition of the BDMA accelerator and mechanically swirled until evenly mixed. The mixture was warmed in a 60°C oven for 15 min to reduce viscosity and 30% weight/weight iron oxide was added to the Epon mixture and vortexed for 1 min. Using a 450 W digital probe sonicator (Branson W-450 D), the mixture was then sonicated at 20% amplitude for 30 min in 5 min intervals with the sonicator probe fully immersed in the scintillation vial. To dissipate heat during sonication the scintillation vial was surrounded in a container with ice-cold water. Following sonication, the accelerator was added and mechanically swirled. We observed equivalent dispersion in other embedding resins including different hardness formulations of Epon as well as Durcupan and Spurr's resins.

### Sample block preparation

To create a cavity for the iron/resin mixture, excess epon was trimmed from one side close to the sample parallel to the cutting direction. The aluminum stub was then surrounded with a tight-fitting thin plastic tubing to create a well. A drop of the freshly prepared iron/resin was then deposited with an insect pin into the cavity. The sample and iron/resin were then cured at 70°C for 24–48 h. To minimize compression along the cutting direction (section length) and to ensure that sections detach from the knife edge and migrate toward the magnet, we shaped the block with pointed leading and trailing edges. This creates a minimal contact area of each section

with the knife edge such that the epon of the previous section does not adhere to the following section or the knife edge. Samples were trimmed with a dry diamond knife to block face sizes approximately 1200–1500  $\mu\text{m}$  long (parallel to the cutting direction) and 750–1000  $\mu\text{m}$  wide including  $\sim 250 \mu\text{m}$  of the iron/resin to the right of the tissue.

### Assembly of collection boats and sectioning procedure

The custom collection boats were machined from aluminum and consist of two parts, a frontend to clamp a diamond knife and a backend collection boat that is sized for either configuration one or two. To assemble the boats, a diamond knife ( $35^\circ$  or  $45^\circ$  Ultra or Ultra Jumbo knives, Diatome) is first clamped into the frontend and held at the manufacturer specified clearance angle (typically  $0^\circ$  or  $6^\circ$ ). The knife edge was then covered with a 3D printed cover and secured in place with a clamping bracket. The rear portion of the knife was then milled to a depth flush with the frontend holder. The milling of knives does not preclude the ability to have them resharpened by the manufacturer (Diatome). The backend collection boat was then screwed to the frontend, and the interface between the diamond knife and backend was made water-tight by applying a thin bead of cyanoacrylic glue. The bottoms of the backend collection boats were fitted with either plastic or glass and sealed with cyanoacrylic glue. For assembly of the boats see [Figure S5](#). All sectioning was performed with a Leica UC7 ultramicrotome.

### Configuration one

For collection with configuration one, a neodymium pot magnet with counterbore hole (ZTN-32; supermagnete) was screwed to a support arm that is attached to a rotary stage (Thorlabs) and XYZ micrometer positioner (Thorlabs). A 70 mm diameter cylindrical neodymium magnet (S-70-35-N; supermagnete) was then held in place by the attraction to the pot magnet. Care should be taken when handling the magnets due to the high field strength. The rotary stage allows the relative angle of the magnets to be fine-tuned with respect to the bottom of the backend collection boat. To prepare for sectioning, a 100 mm diameter, 300  $\mu\text{m}$  thick silicon wafer (BO14072; Siegert Wafer) was first glow discharged (Q150R ES; EMS) to create a hydrophilic surface. The wafer was placed on the bottom and the boat filled with Millipore deionized water. Control of the water level was accomplished via a side port that allowed water to be perfused or withdrawn using a syringe pump (NE-1000; New Era Pump Systems). For repeatable positioning of the magnet below the collection boat, the field XYZ components of the magnetic field strength were measured in a grid pattern from the surface of the boat using a teslameter magnetometer (Projekt Elektronik Teslameter FM3-02). The rate at which sections are drawn toward the backend collection boat depends on the strength of the magnetic field at the knife edge, the section thickness, and the cross-sectional area of iron oxide/resin within each section. To assist sections to move toward the backend and prevent sections from accumulating near the knife edge, an optional air puffer was used. The air puffer consisted of a tapered glass capillary attached to an XYZ translator (Thorlabs) and oriented to puff air at the water surface approximately 1 mm behind the knife edge. This had the effect of drawing sections away from the edge of the knife and pushing them toward the backend collection boat. The air puffer was supplied with house compressed air and was controlled with a solenoid pinch valve (PM-0815W; Takasago Fluidic Systems) that was triggered at the end of each downward swing of the microtome cutting arm. Triggering was achieved by mounting a 3mm infrared beam break sensor (Adafruit) on either side of the microtome cutting arm that was read by a microcontroller (Due; Arduino), which then generated a trigger signal to the pinch valve on each break of the IR beam.

During sectioning, a plastic barrier was placed atop the backend collection boat to reduce the rate of evaporation from the boat as well as prevent dust from falling onto the water surface. Following sectioning, sections were deposited onto the silicon wafer by withdrawing water from the boat at a rate of 5–10 mL/min with the syringe pump. The wafer was then removed from the boat with plastic forceps and any residual water on the surface was evaporated by placing the wafer on a 60°C peltier heating plate (BSH300; Benchmark Scientific) for a few minutes.

### Configuration two

For collection with configuration two, a 32 mm diameter neodymium pot magnet with counterbore hole (ZTN-32; supermagnete) was screwed to a support arm that is attached to a rotary stage (Thorlabs) and XYZ micrometer positioner (Thorlabs). A spherical 40 mm diameter neodymium magnet (K-40-C; supermagnete) was then held in place by the attraction to the pot magnet. Care should be taken when handling the magnets due to the high field strength. The rotary stage allows the relative angle of the magnets to be fine-tuned with respect to the surface of the backend collection boat. To prepare for sectioning a silicon wafer (KristallTechnologie S4974) was cut with a wafer saw to a  $39 \times 42 \text{ mm}^2$  rectangle and hydrophilized (PELCO easiGlow) with a negative polarity to air and 20 mA current for 5 min. The wafer was placed toward the rear of the backend and the boat was filled with deionized water. Control of the water level was accomplished via a side port that allowed water to be perfused or withdrawn using a syringe pump. For repeatable positioning of the magnet above the collection boat, the field XYZ components of the magnetic field strength were measured above the knife edge using a teslameter magnetometer (Projekt Elektronik Teslameter FM3-02). The rate at which sections were drawn toward the backend collection boat depends on the strength of the magnetic field at the knife edge, the section thickness, and the cross-sectional area of iron oxide/resin within each section. For visualization of sections on the water surface during cutting, a USB camera was oriented toward a  $45^\circ$  mirror underneath the boat. When ready to collect sections, the wafer was slid forward underneath the sections and water was withdrawn at a rate of 10 mL/min. The wafer was then removed from the boat with plastic forceps and any residual water on the surface evaporated by placing the wafer on a 60°C peltier heating plate for a few minutes.

### Serial sectioning

The zebrafish eye, stained and embedded as described above, was trimmed to a block face width of 420  $\mu\text{m}$  (including 140  $\mu\text{m}$  of iron oxide/resin) and length of 620  $\mu\text{m}$ . The sample was sectioned with a 35 nm section thickness at a speed of 0.8 mm/s using the configuration 2 collection boat. Three wafers (S4974; KristallTechnologie) cut to 39  $\times$  42 mm squares were collected containing 739, 959, and 894 sections, respectively.

The vibratome section of the mouse olfactory bulb, stained and embedded as described above, was trimmed to a block face width of 1000  $\mu\text{m}$  (including 250  $\mu\text{m}$  of iron oxide/resin) and length of 1500  $\mu\text{m}$ . The sample was sectioned with a 35 nm section thickness at a speed of 1.2 mm/s using the configuration 1 collection boat. Four wafers were collected containing 1983, 1865, 1678, and 1969 sections, respectively.

The presence of iron oxide nanoparticles in the block did not lead to any noticeable damage to diamond knives, as we have used the same diamond knife for multiple large-scale 35 nm serial section experiments. Within an experiment, after every few thousand sections, we move the knife to the right by a couple hundred microns so the left side of the sample block that contains tissue is cut with a fresh knife edge.

### SEM imaging

Both volumes were imaged using a 91-beam multibeam scanning electron microscope (mSEM; Zeiss) with a 15  $\mu\text{m}$  beam pitch. The mSEM was controlled via the Zeiss mSEM API. Regions of interest were defined with a template matching-based segmentation, similar to WaferMapper,<sup>27</sup> of each section on a wafer in MATLAB (Mathworks) and then converted to hexagonal fields of view (mFOVs) using the mSEM API. During SEM imaging, we perform one round of autofocus and autostigmation per section over the iron containing region. Sections were imaged with a 50 ns dwell time, 4 nm pixel size and 1.5 kV landing energy. The zebrafish eye dataset contains (in x,y,z) 67348  $\times$  70125  $\times$  2573 voxels (excluding the surrounding resin) and the mouse olfactory bulb dataset downsampled to 16 nm in x,y contains in (x,y,z) 4000  $\times$  4000  $\times$  7495 voxels.

### Alignment and assembly of 3D EM volumes

#### Preprocessing

2D stitching between individually acquired image tiles (corresponding to individual mSEM beams) was performed by calculating 2D cross correlations between neighboring tiles on the same section. Tile positions were solved for using these translations resulting in a global best fit per section (a least squares solution). 2D-stitched section images were corrected for between-tile gradients or offsets and then assembled by blending the image tiles. Images were then normalized between sections for brightness and contrast, because the section order solving is sensitive to these differences. Further details of the 2D alignment have been previously reported.<sup>22</sup>

#### Order solving

2D-stitched images were downsampled (128 nm) and then SIFT features<sup>15</sup> were detected on each section, with keypoints constrained to the ROI region defined before imaging to eliminate potential spurious descriptor matches from non-tissue containing areas (Figure S3A). An image distance metric was calculated between all sections on a single wafer based on the percentage of matching SIFT features, also known as the inlier ratio method.<sup>17</sup> The section order was then resolved by applying an exact traveling salesman problem solver<sup>28</sup> to this section dissimilarity distance matrix, generating an initial proposed ordering (Figure S3B), as in the method previously proposed by Hanslovsky et al.<sup>17</sup> Note, Templier also utilized a matching SIFT feature approach, but first aligned the images using an affine transform and then used cross-correlation values to form a distance matrix.<sup>6</sup> Hanslovsky et al. subsequently use a second cross-correlation based distance matrix (similar to Templier) and second TSP solving round to correct flips in the ordering that we have not yet implemented.

Bad matches in the proposed ordering were detected as sections that did not fit to an affine transformation with their neighbors. These order problems were then resolved semi-manually. For example, sections that did not fit in the proposed ordering were compared again against all sections, but now as a function of this proposed ordering, and then inserted at minimum locations of the distance metric (Figure S3C). Any sections that suffer from uncorrectable artifacts (e.g., a thin section substantially less than 35 nm and therefore of insufficient contrast) were excluded from the volume at this step. Once the order was solved, sections were aligned by an iterative 3D alignment pipeline.<sup>22</sup>

So that computation of the dissimilarity matrix does not become the rate-limiting step of the alignment, we utilize a GPU-enabled library for dense-multidimensional vector (descriptor) nearest-neighbor searches called FAISS.<sup>23</sup> Our current high performance compute resource includes a CPU-GPU hybrid partition containing 84 nodes with four NVIDIA Quadro RTX 6000 GPUs and 48 cores (4,032 CPU cores) each. Using these resources, the generation of the section dissimilarity distance matrix for the zebrafish retina sample required 1.6 h.

#### Cost estimation

The one-time cost to implement GAUSS-EM is on the order of several thousand dollars which includes machining of the aluminum collection boats (variable based on local manufacturing costs), magnets (\$70–140 per magnet), syringe pump (\$800), microcontroller (\$25), pinch valve (~\$100), hot plate (~\$100–200), and teslameter (~\$3000). The consumable costs are on the order of a couple hundred dollars per experiment consisting solely of the cost of silicon wafers (currently ~\$25/wafer), iron oxide nanoparticles

(\$195/100 g) and embedding resin (\$94/Embed 812 kit). Not included are the costs of common equipment for an electron microscopy facility, such as a commercial ultramicrotome, probe sonicator, glow discharger and diamond knives.

#### **QUANTIFICATION AND STATISTICAL ANALYSIS**

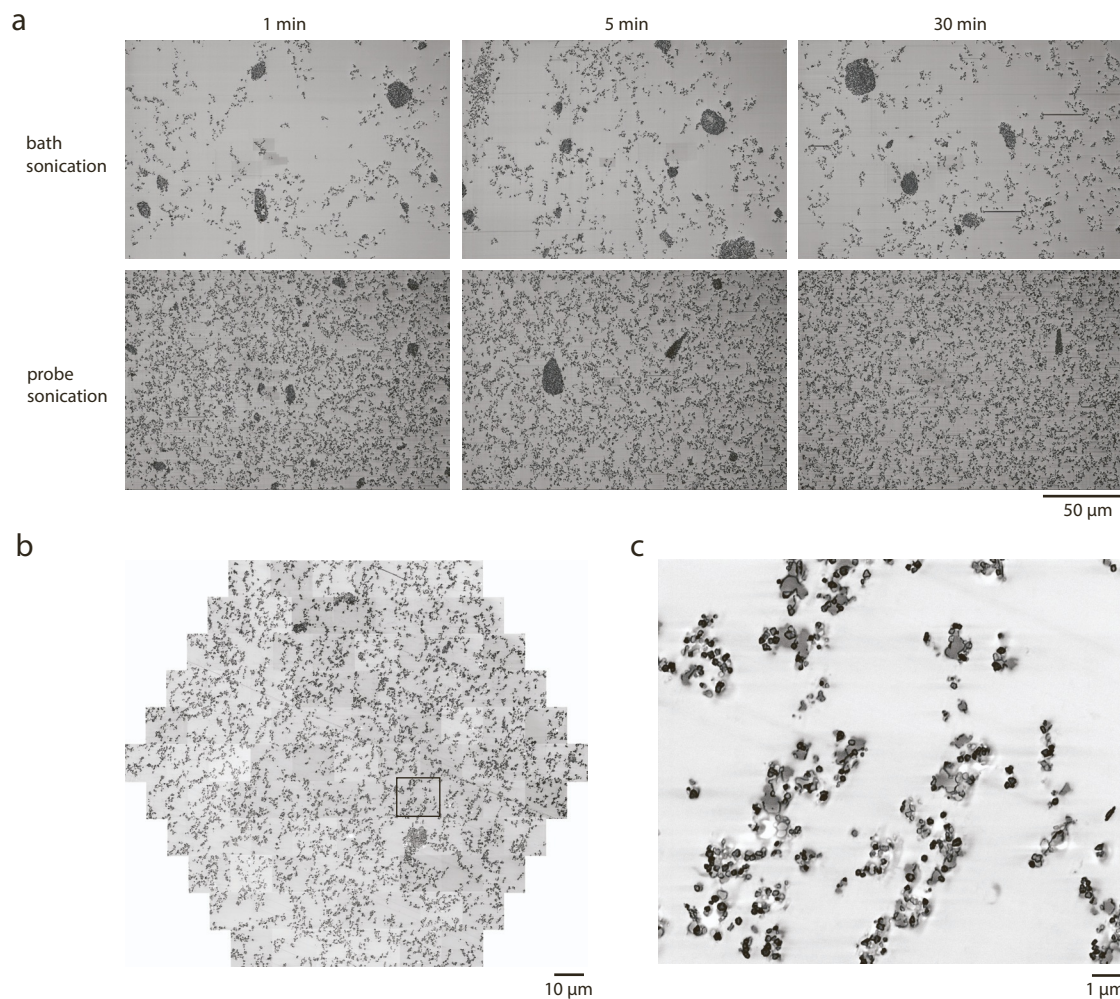
The pipeline to compute the order solving is described above in the corresponding methods subsection *Alignment and assembly of 3D EM volumes*. The methods for evaluating the robustness of the order solving pipeline are provided in the relevant supplemental figure legends and results section.

**Supplemental information**

**GAUSS-EM, guided accumulation of ultrathin  
serial sections with a static magnetic field  
for volume electron microscopy**

**Kara A. Fulton, Paul V. Watkins, and Kevin L. Briggman**

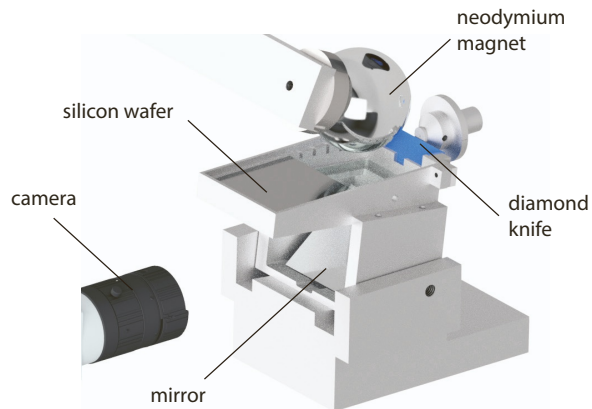
**Figure S1, Related to Figure 1**



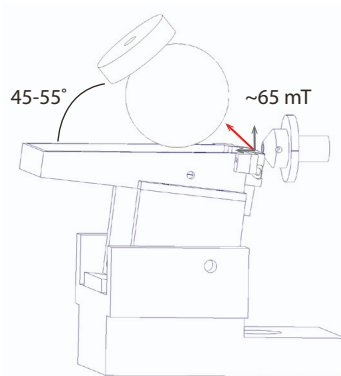
**Figure S1, Dispersion of iron oxide in epoxy resin, related to Figure 1** (a) Electron micrographs of 50 nm thick sections taken from samples in which bath sonication (upper row) or probe sonication (lower row) was used for different durations to disperse iron oxide. (b) mSEM image of 30% iron oxide dispersed in medium hard Epon. (c) Higher magnification of highlighted tile in panel b.

Figure S2, Related to Figure 1

a



b

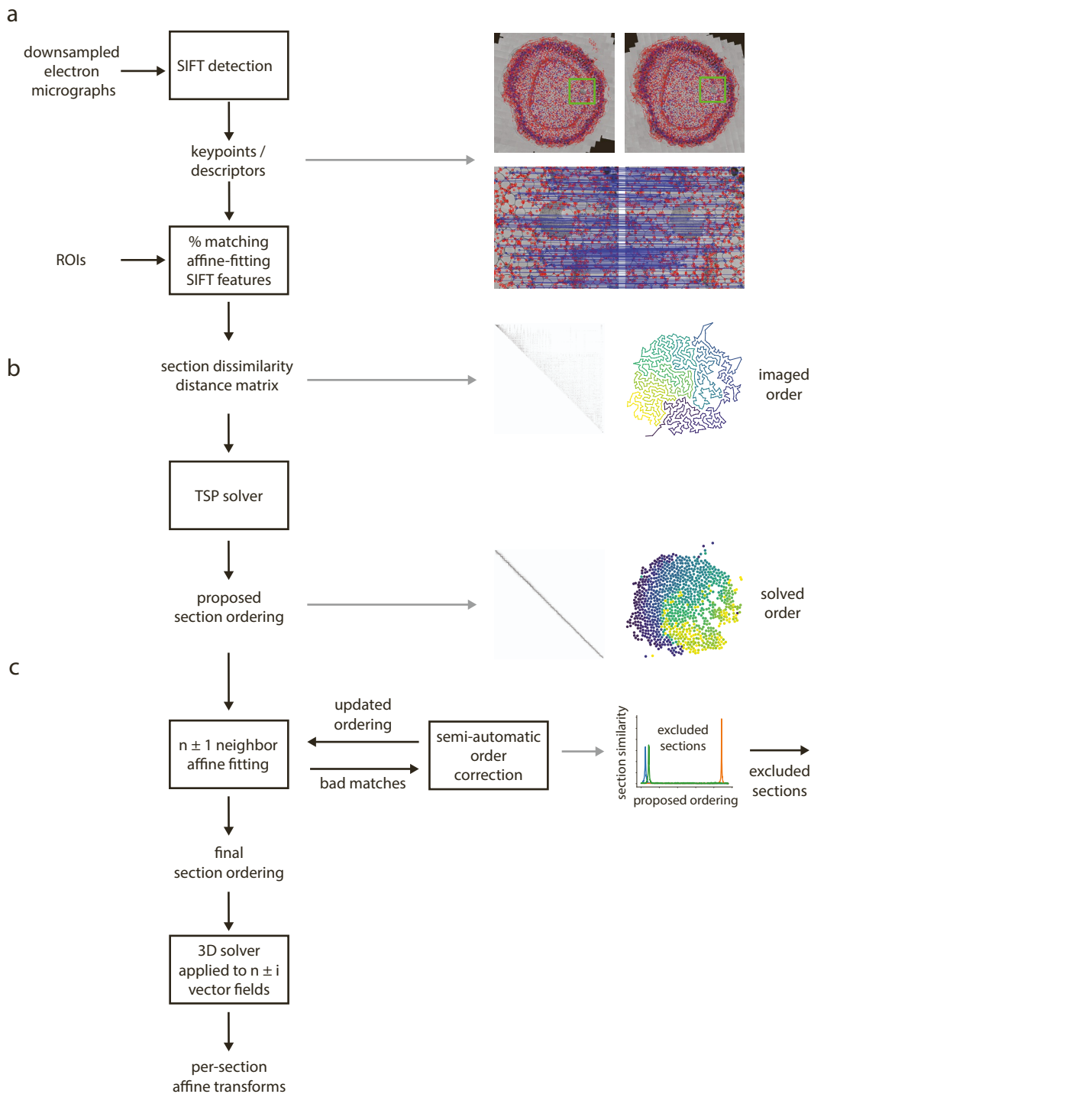


**Figure S2, Configuration two for collecting sections, related to Figure 1 (a)**

Illustration of configuration 2 in which a spherical neodymium magnet is positioned above a custom collection boat designed to accommodate 39 x 42 mm silicon wafers.

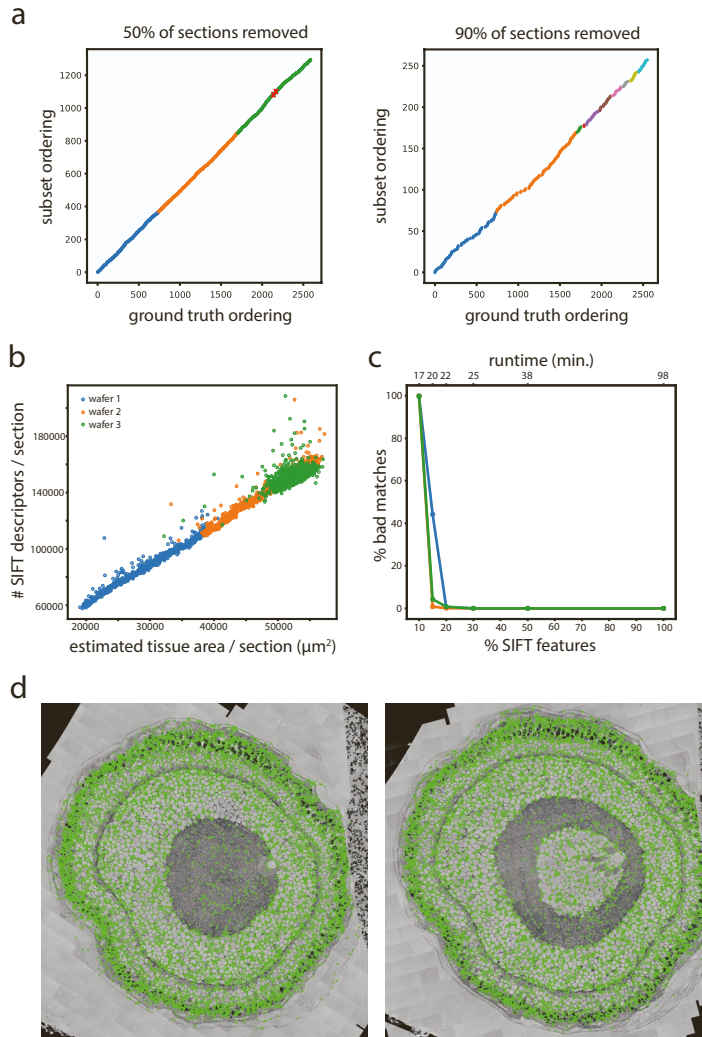
**(b)** Optimal magnet angle and magnetic field strength measured above the diamond knife edge.

Figure S3, Related to Figure 3



**Figure S3, Computational pipeline to solve the order of sections, related to Figure 3** (a) 2D electron micrographs were preprocessed and SIFT features measured from ROIs within each tissue section. Red points indicate detected SIFT features, blue dots and lines indicate matching SIFT features between two sections. A distance matrix was formed among all sections mounted on each wafer using the percent of matching SIFT features as a metric. (b) An initial ordering was proposed using a TSP solver to find the shortest path through the distance matrix. Right panels reproduced from Figure 3b,c. (c) An affine fitting procedure was used to evaluate the proposed order. Any poorly matched sections were semi-automatically placed in the ordering by finding the location of maximum similarity within the proposed ordering. Example shown of placing 3 slices (blue, green, and orange) within the ordering. During this process, sections that are not sufficiently similar to any sections in the proposed ordering can be permanently excluded. The final section ordering was then aligned with a 3D solver to generate a final affine transform per section.

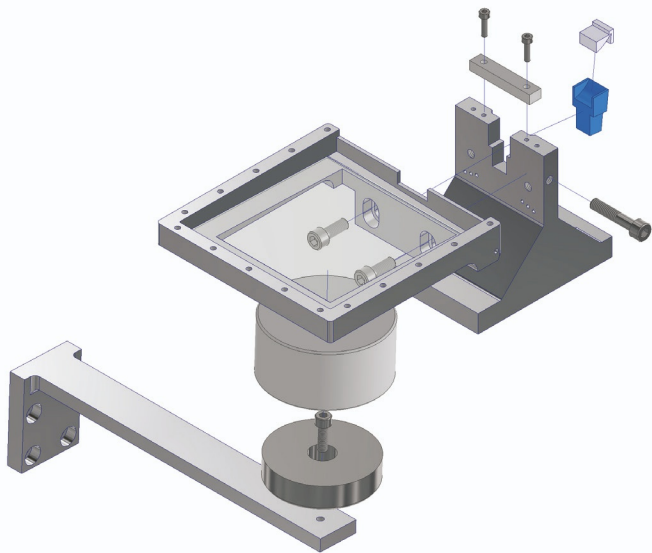
Figure S4, Related to Figure 3



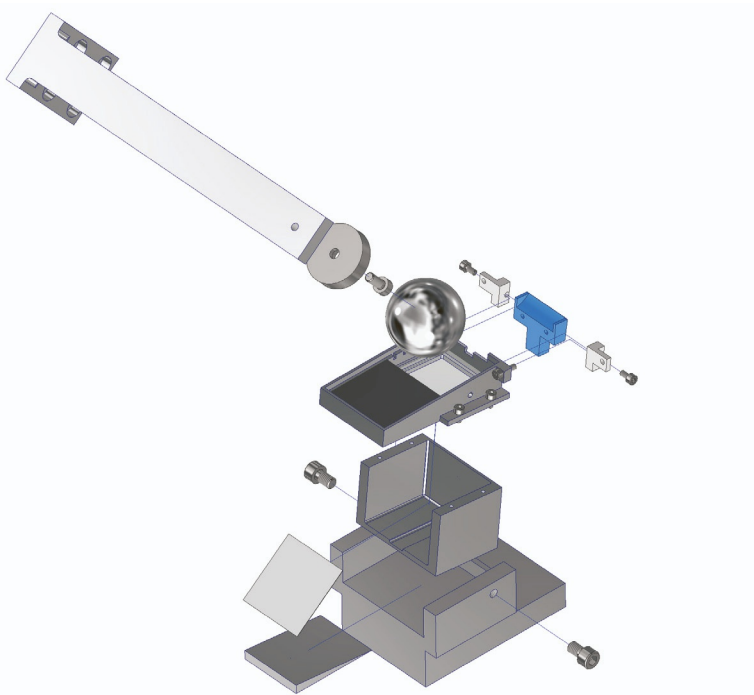
**Figure S4, Robustness of order solving pipeline, related to Figure 3** (a) 50% (left panel) or 90% (right panel) of sections from the zebrafish retina volume were randomly removed and the order solving was repeated for each wafer. The ordering of the remaining sections was in agreement with the original (ground truth) ordering for each wafer, except for two swapped sections (red X's). Colored points indicate the solved segments for each wafer. (b) Correlation between number of descriptive features and tissue area from which feature descriptors were detected ( $r^2 = 0.977$ ,  $p = 0.0$ ). Color dots represent individual sections on three separate wafers from the zebrafish retina volume. (c) The percent of bad match sections plotted against randomly sampled SIFT features. Each wafer is represented by different color lines, as in panel b. Also plotted are the corresponding runtimes to create the section dissimilarity distance matrix. (d) Representative sections illustrating the distribution of matching SIFT features overlaid on top of the tissue structure. Matching SIFT features are distributed more often in somata regions and less frequently in neuropil regions of the sections.

Figure S5, Related to STAR Methods

a



b



**Figure S5, Assembly of custom collection boats, related to STAR Methods** (a) Drawing of the assembly of the configuration 1 collection boat. (b) Drawing of the assembly of the configuration 2 collection boat.